Computational model to address lens-based acoustic field aperture in the in vitro ultrasonic cell stimulation

Elise Doveri, Meysam Majnooni, Carine Guivier-Curien, Cécile Baron, Philippe Lasaygues

Computational model to address lens-based acoustic field aperture in the *in vitro* ultrasonic cell stimulation

https://doi.org/10.1016/j.ultras.2023.107226

Elise Doveri[a], Meysam Majnooni[b], Carine Guivier-Curien[b], Cécile Baron[b,*], Philippe Lasaygues[a]

[a]*Aix Marseille Univ, CNRS, Centrale Marseille, LMA UMR 7031, 4 impasse Nikola Tesla, 13453, Marseille, France*
[b]*Aix Marseille Univ, CNRS, Centrale Marseille, IRPHE UMR 7342, 49 rue Frédéric Joliot-Curie, 13384, Marseille, France*

Abstract

Low-Intensity Pulsed Ultrasound Stimulation (*LIPUS*) is a therapeutic modality used for bone tissue regeneration and healing. Its clinical efficacy is still debated, as the underlying physical phenomena remain poorly understood. The interaction between ultrasonic waves and cells, likely to trigger mechanotransduction inducing bone regeneration, is at the center of scientific concerns on the subject.

In order to get new insights into these phenomena, the development of *in vitro* experiments is a key step but special attentions should be paid concerning to the actual acoustic area covered that has to be sufficiently large and homogeneous. To address this issue, an acoustic lens can be placed on the transducer to improve the homogeneity of the acoustic field over the entire cell culture area. A computational model is developed to test several shapes and heights of acoustic lenses and compare their effectiveness in order to find a compromise between the surface covered, the homogeneity of the intensity distribution and the acoustic pressure loss.

All the lenses studied improve the enlargement of the field and its homogeneity

*Corresponding author
Email addresses: doveri@lma.cnrs-mrs.fr (Elise Doveri), meysam.majnooni@univ-amu.fr (Meysam Majnooni), carine.guivier@univ-amu.fr (Carine Guivier-Curien), cecile.baron@univ-amu.fr (Cécile Baron), lasaygues@lma.cnrs-mrs.fr (Philippe Lasaygues)

but they all generate pressure acoustic loss. The best performing lens in terms of field homogeneity is the one that minimizes pressure acoustic loss but covers only 22% of the target surface. The best enlargement (68% of the surface covered) is obtained for a lens that produces a field that is 4 times less homogeneous and 3 times less efficient in terms of pressure acoustic loss. As no one lens is ideal, the choice of the lens should be the result of a compromise taking into account the prioritization of criteria.

Keywords: LIPUS stimulation, Computational model, Acoustic field aperture, Acoustic lens, Acoustic intensity
https://doi.org/10.1016/j.ultras.2023.107226

---

1. Introduction

Ultrasonic waves can be used for the diagnosis of bone pathologies [1] as well as for therapy, for the removal of kidney stones (lithotripsy) and for the ablation of cancerous tumors. They are also used for bone healing [2], and this work focuses on the investigation of this application. The first clinical observations of the effect of *Low Intensity Pulsed Ultrasound* (*LIPUS*) for bone healing stimulation were reported in the early 1950s [3]. In 1994, the *United States Food and Drug Administration* (*U.S. FDA*) confirmed that *LIPUS* can be used for therapeutic clinical applications and approved clinical devices such as *Exogen* (Smith & Nephew Inc., Memphis, TN, USA), *Osteotron IV* (ITO Physiotherapy & Rehabilitation, Kawaguchi, Saitama, Japan), or *Melmak* (BTT Melmak Development & Production GmbH, Raisting, Germany).

In the literature, the clinical value of *LIPUS* treatment using this kind of devices is currently controversial. Some clinical studies show that the use of *LIPUS* can enhance the healing rate of nonunion fractures [4, 5, 6] and metatarsal fractures [7, 8, 9] whereas other studies show that *LIPUS* has no significant effect on fracture healing [10, 11]. It has also been shown that the effectiveness of *LIPUS* may depend on the patient [12]. One reason why the controversy cannot be resolved is that the underlying mechanisms triggering bone remodeling under *LIPUS* stimulation are still poorly understood [2].

In order to make progress on this issue, *in vitro* setups are key tools to better understand the interaction between *LIPUS* and bone cells. A wide variety of *in vitro* setups with different *LIPUS* stimulation conditions are proposed in the literature [13, 14, 15, 16]. In these papers, the ultrasound signals are in continuous or burst mode, with frequencies between 45 kHz and 3 MHz, with daily exposure times between 1 and 20 minutes, and acoustic intensities between 5 mW/cm^2 and 1 W/cm^2 [17] which makes it difficult to rigorously compare the results obtained. In the present paper, only the frequency of 1 MHz is studied.

One of the challenges in achieving a relevant interpretation of the biological effects consists in the accurate monitoring of the acoustic dose received by the cells in a Petri dish. This monitoring is often mentioned in dedicated literature but rarely satisfactorily performed, because of multiple phenomena disturbing the propagation of the acoustic waves and the cell/wave interactions. Whatever the relative positions of the transducer and Petri dish, or the range of ultrasonic frequencies, one first disturbing effect is related to the standing waves that occur in the cell culture layer inside the Petri dish [18]. These standing waves can be constructive or destructive, and depend on the thickness of the fluid layer with

a precision of a quarter of the wavelength ($\lambda/4$), i.e., a few hundred micrometers in water in the megahertz range [19]. Consequently, it is very difficult to control these experimental conditions and to evaluate the consequences of these phenomena on the measurable acoustic intensity. A technical solution to this problem has been proposed recently [20], consisting of an anti-reflection cover with high performance acoustic absorbing foam that reduces multiple reflections, traps transmitted waves and thus suppresses standing waves. However, even if these disturbing phenomena are neutralized, the acoustic field remains unsatisfactory in terms of spatial distribution (extent and homogeneity) in the Petri dish.

One of the solutions proposed in this work is to develop an acoustic lens that would broaden and homogenize the ultrasonic beam to obtain a targeted distribution of the acoustic intensity inside the Petri dish. For this purpose, a first step consists in the development of a computational model using *Finite Element Method* (*FEM*) to design the size and shape of the lenses, and to study their effects on the acoustic field delivered inside the Petri dish, in terms of broadening, inhomogeneity and acoustic pressure loss.

2. Materials & Methods

2.1. Preamble

The computational model used in this work was based on an experimental setup developed by our group [20, 21]. A Petri dish was positioned on the surface of a water tank, in the far field of a transducer. Placed above the Petri dish, an absorbing cover was used to prevent the formation of standing waves in the water layer inside the Petri dish, as shown in Figure 1(a) (details can be found in [20]).

The spatial distribution of the ultrasound stimulation inside the Petri dish was evaluated by measuring acoustic intensities (Appendix A)[22]. The *Temporal-Average Intensity* (I_{TA}) is defined as follows:

$$I_{\mathrm{TA}} = 1/(ZT_{\mathrm{PRP}}) \int_0^{T_{\mathrm{PRP}}} p(t)^2 \mathrm{d}t \ , \tag{1}$$

where $p(t)$ is the total acoustic pressure, T_{PRP} is the *Pulse Repetition Period* and Z is the acoustic impedance of the medium.

The maximum intensity of I_{TA} over the beam cross-sectional area S defines the *Spatial-Peak Temporal-Average Intensity* (I_{SPTA}), defined as follows:

$$I_{\mathrm{SPTA}} = \max_S(I_{\mathrm{TA}}) \ , \tag{2}$$

making it possible to define a normalized acoustic intensity ($\tilde{I}_{\mathrm{TA}}$) as follows:

$$\tilde{I}_{\mathrm{TA}} = I_{\mathrm{TA}} / I_{\mathrm{SPTA}} \ . \tag{3}$$

2.2. *Computational model*

The computational model was developed in *COMSOL Multiphysics*® v5.5 (Stockholm, Sweden) using the Pressure Acoustics module (transient mode) for the acoustic wave propagation in the fluid parts (water under and inside the dish) and the Solid Mechanics module for the elastic wave propagation inside the Petri dish.

2.2.1. *Geometrical model and mechanical properties*

The computational model was a 2D axisymmetric model, as shown in Figure 1(b).

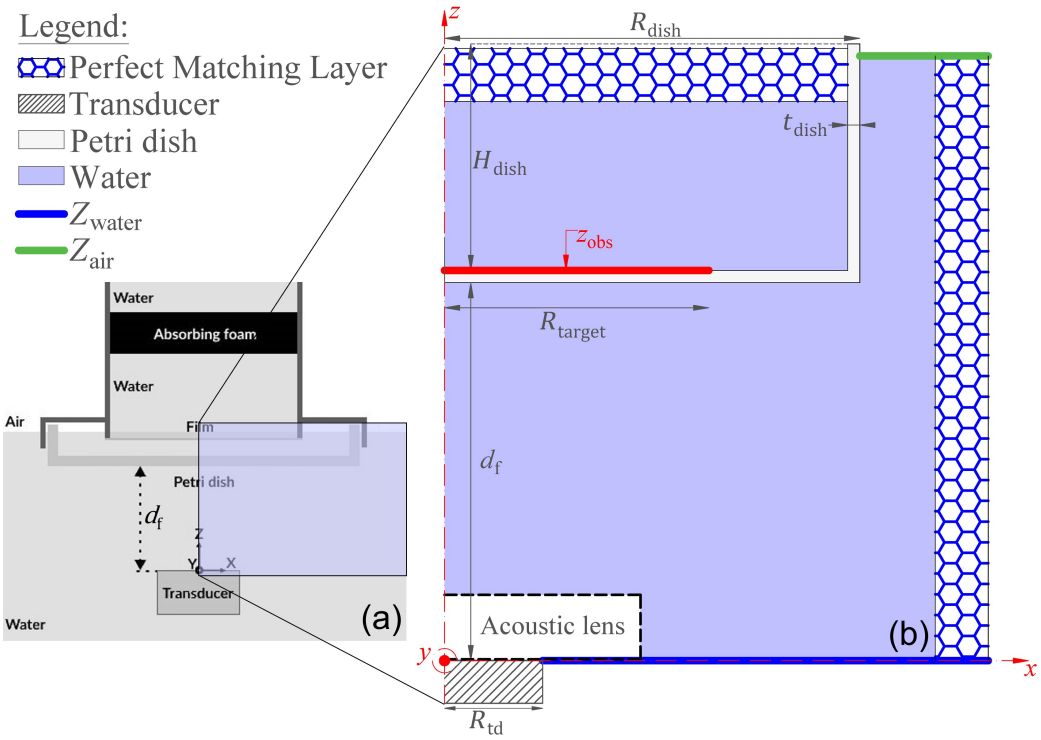

Figure 1: Schematic view of (a) the experimental set-up developed by Majnooni *et al.* [21] and (b) the 2D axisymmetric (around the z-axis) computational model, based on the experimental set-up.

The Petri dish was made of polystyrene (Table 1) and had an external diameter of $D_{\text{dish}} = 2R_{\text{dish}} = 55$ mm, a depth of $H_{\text{dish}} = 15$ mm and a wall and bottom thickness of $t_{\text{dish}} = 0.8$ mm. The targeted area defined as the area intended for cell culture was assumed to be a disk with a diameter of $D_{\text{target}} = 2R_{\text{target}} = 35$ mm [21].

Material	Young Modulus E [GPa]	Poisson's ratio ν	Mass density ρ [kg/m^3]	Compression wave velocity V_{L} [m/s]	Shear wave velocity V_{T} [m/s]	Impedance Z [MRayls]
Polystyrene	3.6	0.34	1050	2367	1131	2.49

Table 1: Characteristics of the polystyrene which composes the Petri dish [23]

The transducer was supposed to radiate as a plane piston of $D_{\text{td}} = 2R_{\text{td}} = 13$ mm diameter. The distance d_{f} between the transducer and the Petri dish had been set at 25 mm. The horizontal red line in Figure 1(b) corresponds to the distance of observation $z_{\text{obs}} = 25.81$ mm (which is the position of the cells inside the Petri dish), as in [21]. The distance d_{f} and the transducer diameter D_{td} are constrained by the dimensions of the incubator provided in the associated experimental set-up [21]. Previous results obtained by Majnooni *et al.* [21] showed that, with this configuration, most of the targeted area is not insonified.

2.2.2. Acoustic lens geometry

The lens used to broaden the aperture angle and homogenize the ultrasonic beam was positioned above the transducer. Three shapes of lenses were tested. The first lens was a spherical cap made of epoxy resin (noted E-lens from now on) [Fig. 2(a)].

To cover the entire active front face of the transducer, the width of the epoxy resin cap was set such that $L_{\text{epoxy}} = D_{\text{td}} + 2$ mm $= 15$ mm. Its height H_{epoxy} and its curvature radius R_{epoxy} are related by the following equation:

$$R_{\text{epoxy}} = H_{\text{epoxy}}/2 + L_{\text{epoxy}}^2/(8H_{\text{epoxy}}) \ . \tag{4}$$

In the present work, H_{epoxy} is set as a variable, in order to study how it affects the ultrasonic fields and the acoustic intensity distribution inside the Petri dish.

Because the acoustic impedance in the epoxy resin was higher than in water (Table 2), a fraction of the wave energy was reflected from the lens/water interface. To reduce this effect, a second type of lens was designed (noted S-lens,

for spherical lens, from now on): the epoxy resin cap was surrounded by a layer of *polydimethylsiloxane* (*PDMS*) with a constant thickness of 1 mm [Fig. 2(b)]. *PDMS*, with an acoustic impedance (Table 2) closer to that of water, acted as an acoustic impedance matching layer, allowing more energy to be transmitted through the lens.

The third lens design (noted C-lens, for cylindrical lens, from now on) was also a cap-shaped epoxy resin lens with a cylindrical top layer of *PDMS* forming a flat interface with water, as shown in Figure 2(c). This lens was similar to the one developed by Yang *et al.* [24].

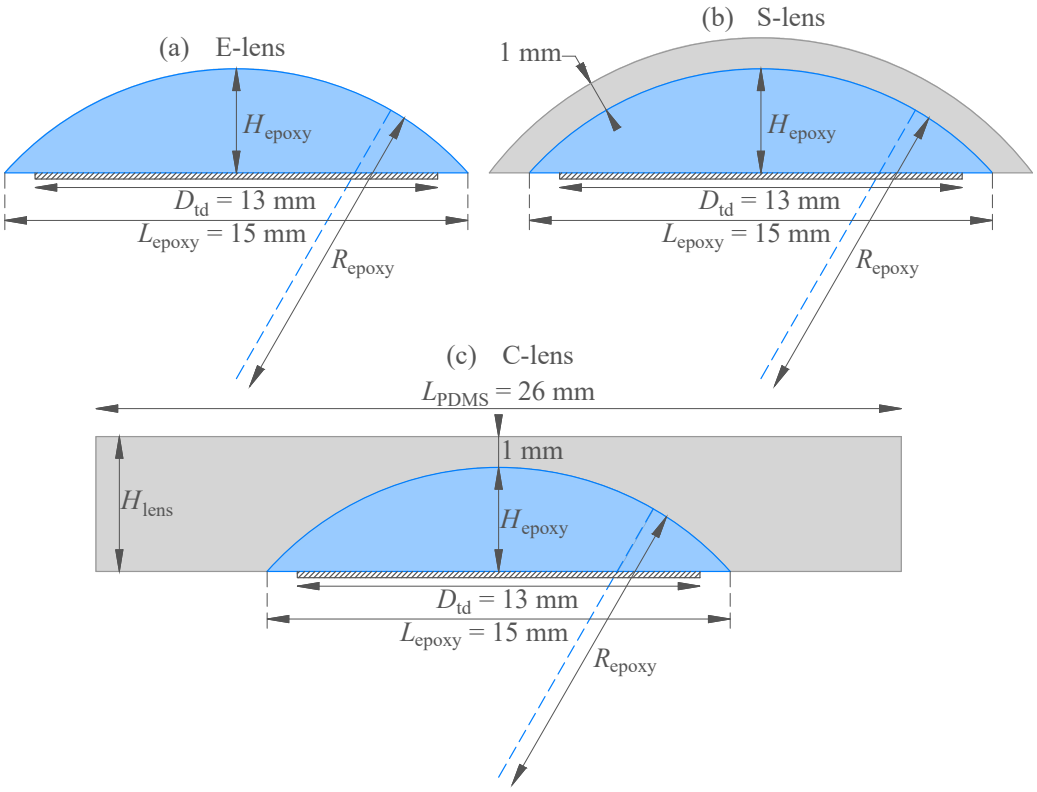

Figure 2: Schematic view of (a) the E-lens, (b) the S-lens and (c) the C-lens

The *PDMS* used was the *Sylgard*^{TM} *184* (Dow Corning, Midland MI). The acoustic properties of the *PDMS* and of the epoxy resin are given in Table 2.

Material	Mass density ρ [kg/m^3]	Compression wave velocity V_{L} [m/s]	Impedance Z [MRayls]	Compression attenuation coefficient α_{L} at 1 MHz [dB/cm]	Shear attenuation coefficient α_{T} at 1 MHz [dB/cm]
Water (17.8^{o}C) [20]	1000	1474	1.47	$2.2\ 10^{-3}$	-
Sylgard 184 [25]	1031	1030	1.06	1.91	1499
Epoxy [26]	1080	2300	2.48	5.32	30

Table 2: Acoustic properties of water, *PDMS* and epoxy resin. The given values are mean values obtained from the literature. The values for water are the ones of a previous experiment [20]. The values for epoxy are for an Araldite 2011 epoxy material (Huntsman Advanced Materials, Everberg, Belgium) [26].

The *PDMS* and the epoxy resin were assumed to be fluid because the attenuation coefficients of the shear waves α_{T} inside them were much higher than the attenuation coefficients of the compression waves α_{L} (Table 2). There was a small space of water (0.1 mm) between the transducer and the lens in order to mimic the fact that the lens was not directly in contact with the transducer.

2.2.3. Transmitted signal

The incident acoustic pressure $P(t)$ was defined as follows:

$$P(t) = P_0 \sin(2\pi f_0 t)\ , \tag{5}$$

$$\text{with} \begin{cases} P_0 = P_{\max} & \text{for } 0 \leq t \leq t_{\mathrm{pulse}} = 200\ \mu\mathrm{s}, \\ P_0 = 0\ \mathrm{kPa} & \text{for } t_{\mathrm{pulse}} = 200\ \mu\mathrm{s} < t \leq T_{\mathrm{PRP}} = 1\ \mathrm{ms}, \end{cases}$$

where P_0 was the amplitude of the transmitted signal, $f_0 = 1$ MHz the nominal frequency of the transmitted wave, and t the time variable. Note that by definition $\tilde{I}_{\mathrm{TA}}$, in Equation (3), does not depend on the $P_{\max}$ value.

2.2.4. Boundary conditions

In order to model an infinite medium of water around the Petri dish, a *Perfect Matching Layer* (*PML*) was placed on the right side of the model [blue honeycomb in Figure 1(b)]. To simulate the effect of the absorbing cover on top of the Petri dish, there was also a *PML* at this interface.

To mimic the air above the top right-end water layer, the boundary condition was the impedance of air (Z_{air}) [top-right green line in Fig.1(b)].

Because the experimental set-up [Fig.1(a)] was immersed in a water tank, the bottom boundary condition of the computational model was supposed to be water layers with an acoustic impedance (Z_{water}) [blue lines in Fig.1(b)].

2.2.5. Mesh

The mesh size was homogeneous in all the materials of the model. It was such that there were at least 8 elements per smallest wavelength.

In the water and Petri dish, the mesh was made with free quads and in the lens it was made with free triangles. The time step of the simulation was defined as follows:

$$\Delta t = \Delta x_{\min}/(\sqrt{2}V_{\max}) \ , \tag{6}$$

with $\Delta x_{\min}$ was the smaller mesh size and $V_{\max}$was the maximum wave velocity. This led to a *Courant–Friedrichs–Lewy* (*CFL*) condition equal to $1/\sqrt{2} \approx 0.7$, which was smaller than 1, ensuring the stability of the numerical scheme.

2.2.6. Wave attenuation

The Petri dish was considered as an elastic solid. However, the wave attenuation inside the walls was not taken into account. In fact, the attenuation coefficient of the compression wave in polystyrene being 1.36 dB/cm [23] and the thickness of the walls being 800 μm, the attenuation due to the Petri dish was assumed negligible compared with the one due to the lens. Only the wave attenuation in the fluid parts (acoustic lens and water) was taken into account using *General dissipation* for the fluid model [27], which requires to define the sound diffusivity δ as [28]:

$$\delta = \nu[\phi/\mu_{\rm s} + (\gamma - 1)/P_{\rm r}] \ , \tag{7}$$

with:

- $\nu = \mu_{\rm s}/\rho$, the kinematic viscosity [m^2/s],
- $\mu_{\rm s}$, the shear viscosity [Pa.s],
- ρ, the mass density [kg/m^3],
- $\phi = 4\mu_{\rm s}/3 + \mu_{\rm b}$, the longitudinal viscosity [Pa.s],
- $\mu_{\rm b}$, the bulk viscosity [Pa.s],
- γ, the ratio of specific heats,
- $P_{\rm r} = \nu/a$, the Prandtl number,
- a, the thermal diffusivity [m^2/s].

The coefficient of sound attenuation $\alpha_{\mathrm{L}}^{\mathrm{Np}}$ (expressed in Np/m) is defined as [29]:

$$\alpha_{\mathrm{L}}^{\mathrm{Np}} = [\phi + \rho a(\gamma - 1)]\omega^2/(2\rho V_{\mathrm{L}}^3) \ , \tag{8}$$

with:

- V_{L}, the compression wave velocity in the fluid [m/s],
- $\omega = 2\pi f_0$, the pulsation [rad/s],
- f_0, the working frequency [Hz].

Finally, when combining Eq. (7) with Eq. (8), the sound diffusivity was defined in terms of the compression wave attenuation coefficient:

$$\delta = 2V_{\mathrm{L}}^3\alpha_{\mathrm{L}}^{\mathrm{Np}}/\omega^2 = 2V_{\mathrm{L}}^3\alpha_{\mathrm{L}}/[20\log(\mathrm{e}^1)\omega^2] \approx 0.23V_{\mathrm{L}}^3\alpha_{\mathrm{L}}/\omega^2 \ , \tag{9}$$

with α_{L} the compression wave attenuation coefficient expressed in dB/m. Table 3 gives the sound diffusivity at $f_0 = 1$ MHz, for each fluid material.

Material	Sound diffusivity δ [cm^2/s]
Water (17.8^{o}C)	0.04
Sylgard 184	12
Epoxy	378

Table 3: Sound diffusivity at $f_0 = 1$ MHz, for each fluid material

2.3. Criteria of effectiveness

2.3.1. Aperture ratio

In order to characterize the broadening of the field aperture, three different areas were defined [Fig. 3] inside the Petri dish:

- The targeted area [Fig.3(a)], which corresponds to the area intended for cell culture in the *in vitro* set-up [21]. It is a disk of radius $R_{\mathrm{target}} = D_{\mathrm{target}}/2 = 17.5$ mm.
- The insonification area [Fig.3(b)], which corresponds to the area where the acoustic intensity is not zero. It is a disk of radius R_{ins}.
- The beam area [Fig.3(c)], which corresponds to the area where $\tilde{I}_{\mathrm{TA}}$ is greater than 0.25 (details can be found in Appendix A).

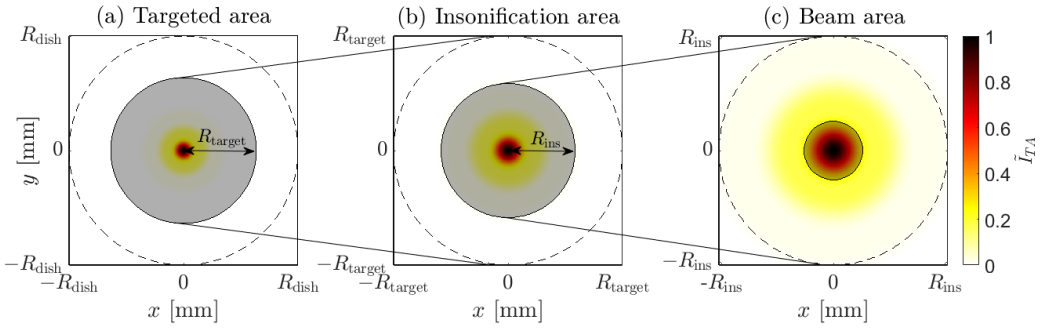

Figure 3: Representations of (a) the targeted area, (b) the insonification area and (c) the beam area, based on the normalized intensity $\tilde{I}_{\text{TA}}$ calculated in the absence of lens, at a distance of $z_{\text{obs}} = 25.81$ mm, on the x/y plane

Finally, an *aperture ratio* (expressed in %) was introduced as the ratio of the beam area over the targeted area. One of the aims of this study was then to design an acoustic lens that provides a beam area equal to the targeted area, in order to obtain an *aperture ratio* of 100%.

2.3.2. Inhomogeneity

In order to quantify the *inhomogeneity* of the intensity distribution inside the Petri dish, the mean value and the standard deviation of the absolute value of the gradient of $\tilde{I}_{\text{TA}}$ were calculated [15]. The absolute value of the gradient of the $\tilde{I}_{\text{TA}}$ was defined (more details in Appendix A) as:

$$\left|\nabla \tilde{I}_{\text{TA}}\right| = \left|\frac{\partial \tilde{I}_{\text{TA}}}{\partial x}\right| + \left|\frac{\partial \tilde{I}_{\text{TA}}}{\partial y}\right| . \tag{10}$$

The mean value and the standard deviation of $|\nabla \tilde{I}_{\text{TA}}|$ give information about, respectively, the number and the amplitude of oscillations of the intensity distribution. An homogeneous acoustic intensity field means that the mean value and the standard deviation of $|\nabla \tilde{I}_{\text{TA}}|$ are equal to 0.

2.3.3. Pressure acoustic loss

In order to estimate the wave attenuation induced by the different shapes of lens, the pressure acoustic loss (PAL, expressed in dB) due to each lens was calculated by multiplying the attenuation coefficient of each lens material (epoxy

or PDMS) of the lens (Table 2) by the distance traveled by the wave inside each corresponding part of the lens :

$$\begin{cases} PAL = \alpha_{\mathrm{L}}^{\mathrm{epoxy}} d_{\mathrm{epoxy}} \text{ , for the E-lens,} \\ PAL = \alpha_{\mathrm{L}}^{\mathrm{epoxy}} d_{\mathrm{epoxy}} + \alpha_{\mathrm{L}}^{PDMS} d_{PDMS} \text{ , for the S-lens and the C-lens,} \end{cases} \tag{11}$$

where $\alpha_{\mathrm{L}}^{\mathrm{epoxy}}$ and $\alpha_{\mathrm{L}}^{PDMS}$ are respectively the compression attenuation coefficients of epoxy and *PDMS* (given in Table 2), and where d_{epoxy} and d_{PDMS} are respectively the distances traveled inside epoxy and *PDMS* by a ray starting at the end of the transducer (at $x = D_{\mathrm{td}}/2 = 6.5$ mm) drawn in red on Figure 4.

2.4. Analytical modeling of the aperture angle

The computational model allowed us to quantify the effect of lenses on the broadening of the *aperture angle*, the acoustic field *inhomogeneity*, and the *acoustic pressure loss*. The *aperture angle* can be assessed analytically. Such assessment can thus participate in partially validating the computational model and rapidly quantify the influence of the lens geometry on the aperture angle, especially the optimal value of H_{epoxy}. An analytical modeling (details can be found in [30]) was implemented to compare the aperture of the acoustic field with and without the shaped lenses.

For all the lenses, the first enlargement of the field was due to the epoxy part. Noting θ_1 the incident angle and θ_2 the refracted angle at the epoxy/PDMS interface (or at the epoxy/water interface in the case of the E-lens) :

$$\theta_1 = \arcsin[D_{\mathrm{td}}/(2R_{\mathrm{epoxy}})] \text{ ,} \tag{12}$$

$$\theta_2 = \arcsin(n_1 \sin\theta_1) \text{ ,} \tag{13}$$

with $n_1 = V_{\mathrm{PDMS}}/V_{\mathrm{epoxy}}$ in the cases of the C-lens and S-lens, and $n_1 = V_{\mathrm{water}}/V_{\mathrm{epoxy}}$ in the case of the E-lens, and with V_{PDMS}, V_{epoxy} and V_{water} respectively the compression wave velocities in the *PDMS* layers, in the epoxy resin cap and in the water.These values are given in Table 2.

For the E-lens the aperture is characterized by the angle $\theta_1 - \theta_2$.

For the PDMS/water interface, the angle of incidence θ_3 (represented in Figure 4) was calculated using Snell's law. Assuming that the *PDMS* layer was thin, this angle was written as follows:

$$\theta_3 \approx \theta_2 \text{ , for S-lens,} \tag{14}$$

$$\theta_3 = \theta_1 - \theta_2 \text{ , for C-lens,} \tag{15}$$

Finally the refraction angle at the PDMS/water interface θ_4 is given by:

$$\theta_4 = \arcsin(n_2 \sin\theta_3) \text{ with } n_2 = V_{\text{water}}/V_{\text{PDMS}} \ , \tag{16}$$

with V_{PDMS} and V_{water} the compression wave velocities in the *PDMS* layers and water, respectively. These values are given in Table 2.

The *aperture angle* is $\theta_1 - \theta_4$ for the S-lens, and θ_4 for the C-lens.

The algorithm was implemented using *Matlab*®(The MathWorks, Inc., Natick, MA, USA).

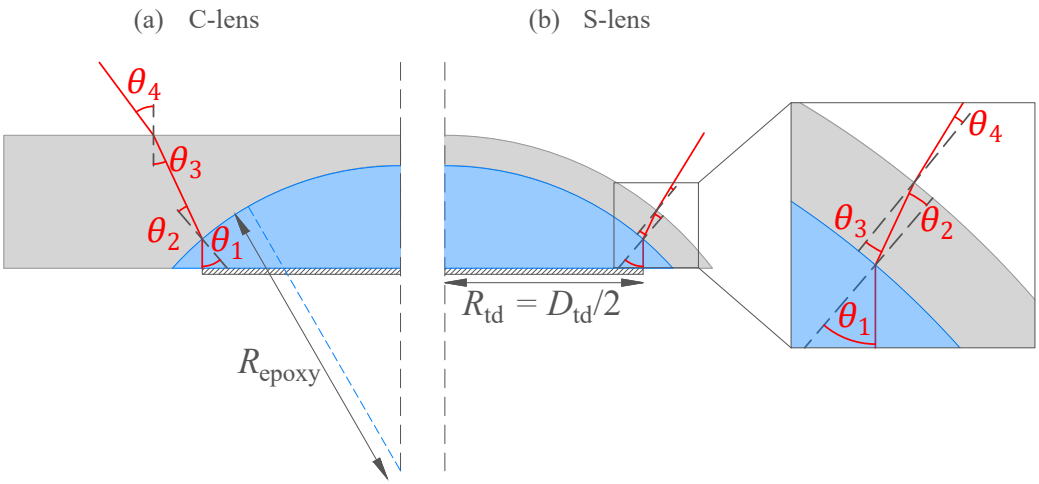

Figure 4: Schematic view of the angular orientation of the beam inside (a) the C-lens and (b) the S-lens.

3. Results and discussion

3.1. Optimal design of the lens

The analytical modeling presented in Section 2.4 was used to determine the appropriate range of H_{epoxy} values for each shape of lens. The minimum and maximum values of H_{epoxy} were determined as follows:

- The minimum value of the H_{epoxy} range was set such that an aperture of 30% of the targeted area ($S_{\text{ins}} = 30\% S_{\text{target}} = 289\ \text{mm}^2$, which corresponds to $R_{30\%} = 10\ \text{mm}$) was reached.

- The maximum value of the H_{epoxy} range was set such that an aperture of 95% of the Petri dish area ($R_{\text{max}} = 26.8$ mm) was reached, or when the maximum of the insonification radius R_{ins} [Fig.3(b)] was reached.

For the three lens shapes, Figure 5 shows:

1. the insonification radius R_{ins} as a function of H_{epoxy} between 0 and 7.5 mm in thick black line,
2. the minimum and maximum thresholds $R_{30\%}$ and R_{max} in black dashed lines,
3. the radius of the targeted area R_{target} in black dotted line.

The minimum (blue vertical lines) and maximum (red vertical lines) values for the H_{epoxy} range are shown for each lens in Figure 5. On each side of a graphic are represented the insonification areas along the z-axis for each lens: in blue for $R_{30\%}$ (the minimum value of the range), and in red for R_{max} (the maximum value of the range).

Table 4 shows the H_{epoxy} values that were chosen to be equi-distributed over the previous range. They were used in the computational model to explore the influence of H_{epoxy} on the *aperture angle* of the lens, the *inhomogeneity* of the intensity distribution inside the Petri dish, and the *pressure acoustic loss* due to the lens.

The selected H_{epoxy} for the E-lens and the S-lens are similar, while the selected ones for the C-lens are different. This means that the *PDMS* layer of the S-lens has a smaller effect on the increase in the insonification radius than the *PDMS* layer of the C-lens.

Shape of lens	H_{epoxy} [mm]
E-lens	[1.70 ; 2.98 ; 4.25 ; 5.53 ; 6.80]
S-lens	[1.00 ; 2.35 ; 3.70 ; 5.05 ; 6.40]
C-lens	[0.80 ; 1.63 ; 2.45 ; 3.28 ; 4.10]

Table 4: Five selected H_{epoxy} values for each shape of lens

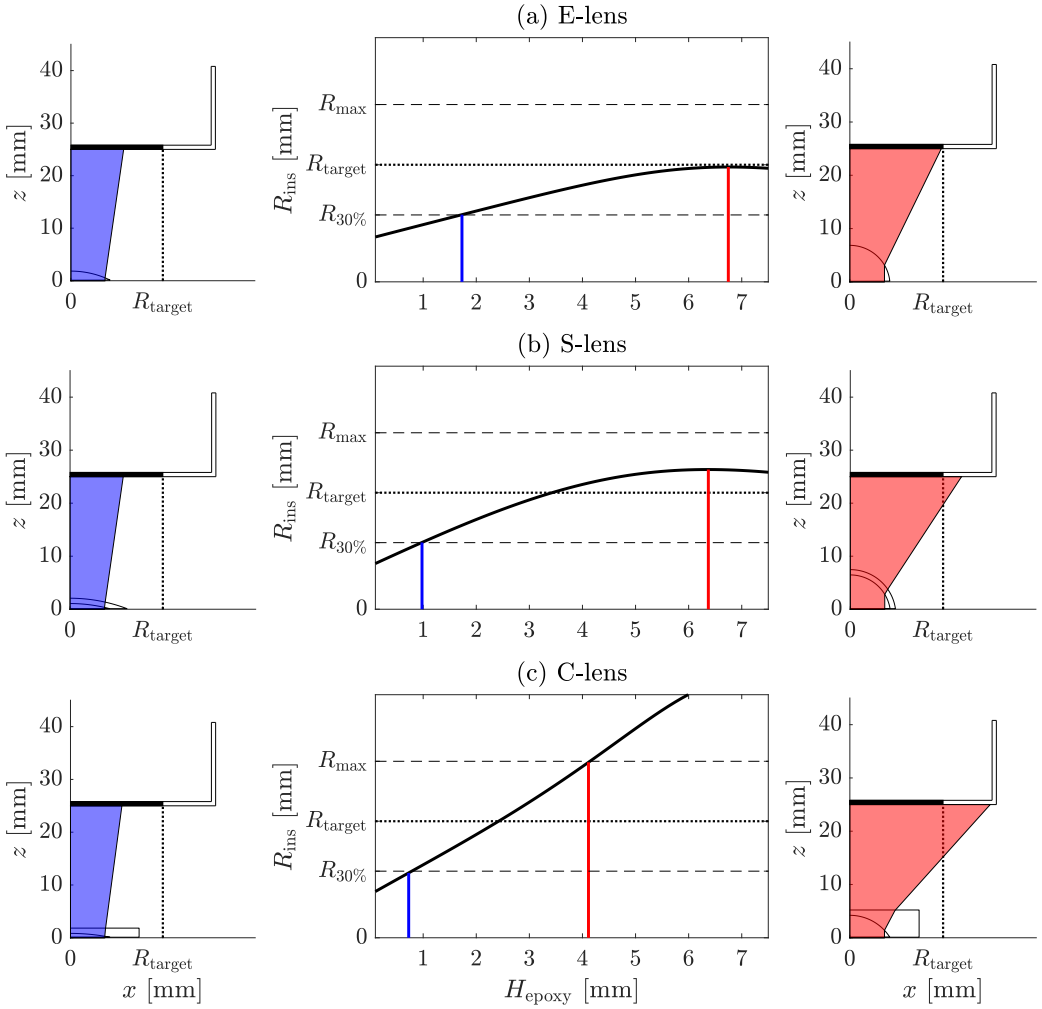

Figure 5: Insonification radius for (a) the E-lens, (b) the S-lens and (c) the C-lens, as a function of the height of the epoxy lens H_{epoxy}. The black dashed horizontal lines correspond to the two thresholds ($R_{30\%} = 10$ mm and $R_{\text{max}} = 26.8$ mm). The black dotted horizontal line corresponds to the radius of the targeted area $R_{\text{target}} = 17.5$ mm. The blue vertical lines correspond to the values of H_{epoxy} that match an insonification radius of $R_{30\%}$. The red vertical lines correspond to the values of H_{epoxy} that match an insonification radius of R_{max} or the maximum value of the insonification radius. On both sides of each graphic are represented the insonification areas along the z-axis, for the corresponding lenses. The blue ones correspond to a H_{epoxy} that matches an insonification radius of $R_{30\%}$. The red ones correspond to a H_{epoxy} that matches an insonification radius of R_{max} or the maximum value of the insonification radius.

3.2. Acoustic intensity distribution along the z-axis

To better understand the influence of the lenses on the acoustic intensity distribution, the results of the analytical model (presented in 2.4) and those of the computational model were overlaid for $\tilde{I}_{\mathrm{TA}}$ along the z-axis (Figure 6). The comparisons are performed for the minimum and maximum of the H_{epoxy} range (Table 4). The vertical black line at $x = 17.5$ mm corresponds to R_{target}.

In order to see small details in the $\tilde{I}_{\mathrm{TA}}$ distributions, the colormap of Figure 6 was shifted, so that when the $\tilde{I}_{\mathrm{TA}}$ is higher than 1%, pixels are coloured in black, so the maximum value of the colormap is set to 1% and the pixels corresponding to an $\tilde{I}_{\mathrm{TA}}$ between 1% and 100% are all coloured in black. This figure validates the analytical model, since the simulated insonification area (in black) corresponds to the analytical insonification area (delimited by the thick red lines).

On the bottom line graphs (d to f) of Figure 6, oscillations can be seen around the Petri dish. These oscillations appear more clearly in the zoom part of Figure 6(f), where a maximum of intensity can be found at the center of the Petri dish and where oscillations can be seen on the interior surface of the dish bottom. This type of $\tilde{I}_{\mathrm{TA}}$ distribution can be related to the work of Hensel *et al.* [31] assuming that when the transducer diameter is close to the Petri dish diameter, "a ring-shaped pattern with maximum acoustic pressure at the well center can be observed". According to them, when the transducer diameter is larger than the Petri dish diameter, acoustic pressure waves are coupled into the Petri dish walls with compression and shear wave components. Then, these waves are transmitted through the liquid and are reflected by the Petri dish walls several times, resulting in constructive superposition at the Petri dish center. In our case, as the lens enlarges the acoustic field sufficiently to insonify almost all the Petri dish bottom [Fig. 6(f)], this effect may occur, which could explain the peak of $\tilde{I}_{\mathrm{TA}}$ at the center of the Petri dish, and the small oscillations aorund it. This central peak is also increased by the axi-symmetry of the Petri dish, which "favors the formation of a symmetric and tapered focus along the central vertical axis" [32].

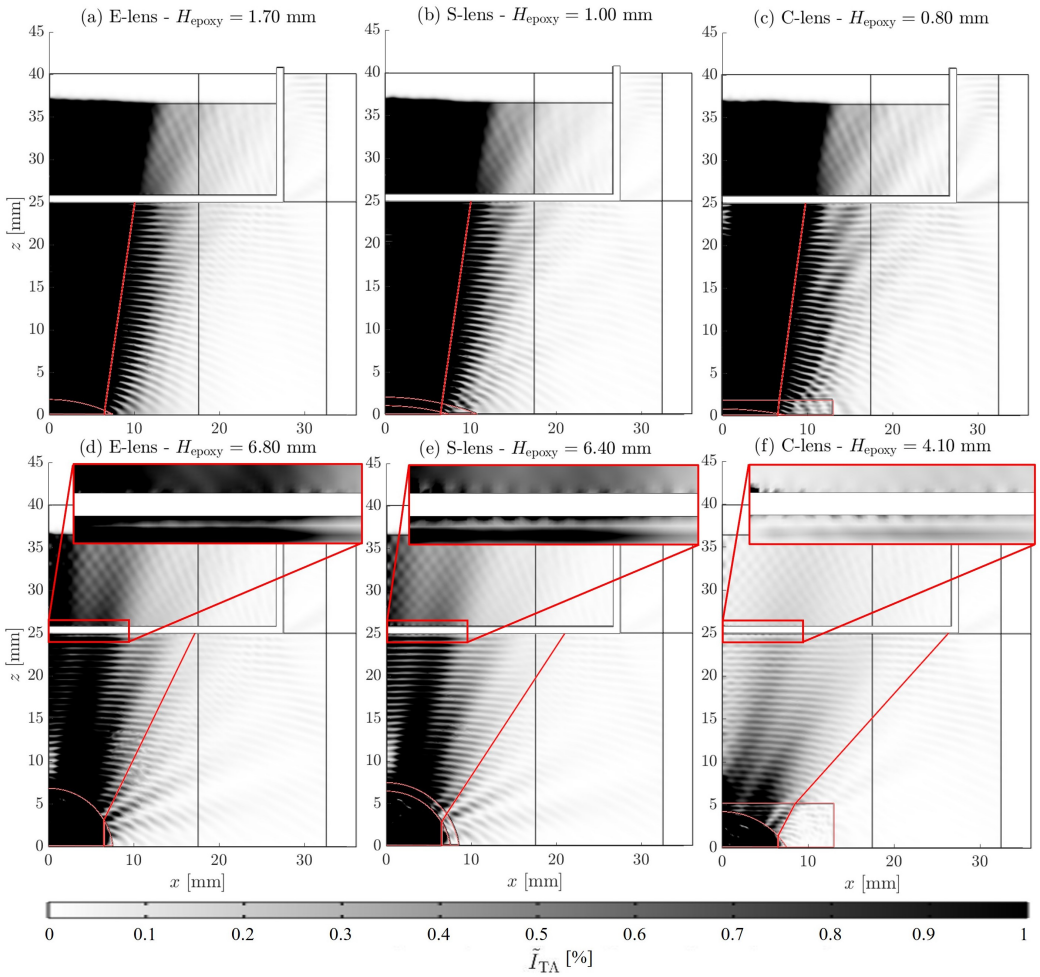

Figure 6: Ray traces obtained by the analytical modeling (thick red lines) overlayed over the $\tilde{I}_{\text{TA}}$ obtained by the computational model along the z-axis, for the minimum and the maximum of the H_{epoxy} range (Table 4), for (a and d) the E-lens, (b and e) the S-lens, and (c and f) the C-lens. The corresponding lenses are drawn in red. On top of the bottom line graphics are plotted zooms of the $\tilde{I}_{\text{TA}}$ close to the bottom of the Petri dish.

3.3. Acoustic intensity along the radius of the Petri dish

In order to understand how the acoustic intensity was distributed inside the Petri dish according to the different designs of the lens, the $\tilde{I}_{\text{TA}}$ was calculated on a plane perpendicular to the z-axis at $z_{\text{obs}} = 25.81$ mm, for each size and each shape of lens. This height corresponds to the place where the cells will be during

the in vitro stimulation. The area where $\tilde{I}_{\mathrm{TA}}$ is plotted corresponds to the targeted area [as defined in Fig. 3(a)].

Figure 7 shows $\tilde{I}_{\mathrm{TA}}$ along the radius of the Petri dish, for different H_{epoxy}, in the case of the C-lens. On all curves, there is a main peak that far exceeds all other peaks in the center of the dish. But, as this peak represents only 0.04 % of the targeted area (corresponding to the blue area of 0.35 mm radius in Fig.7), and as the purpose of this study is to investigate the *inhomogeneity* of the acoustic intensity distribution inside the Petri dish on all the targeted area (and not only on the peak area), we have chosen to remove this peak area from the following results. Omitting this peak in the $\tilde{I}_{\mathrm{TA}}$ distribution thus leads to define a larger beam area than the one that would otherwise be assessed.

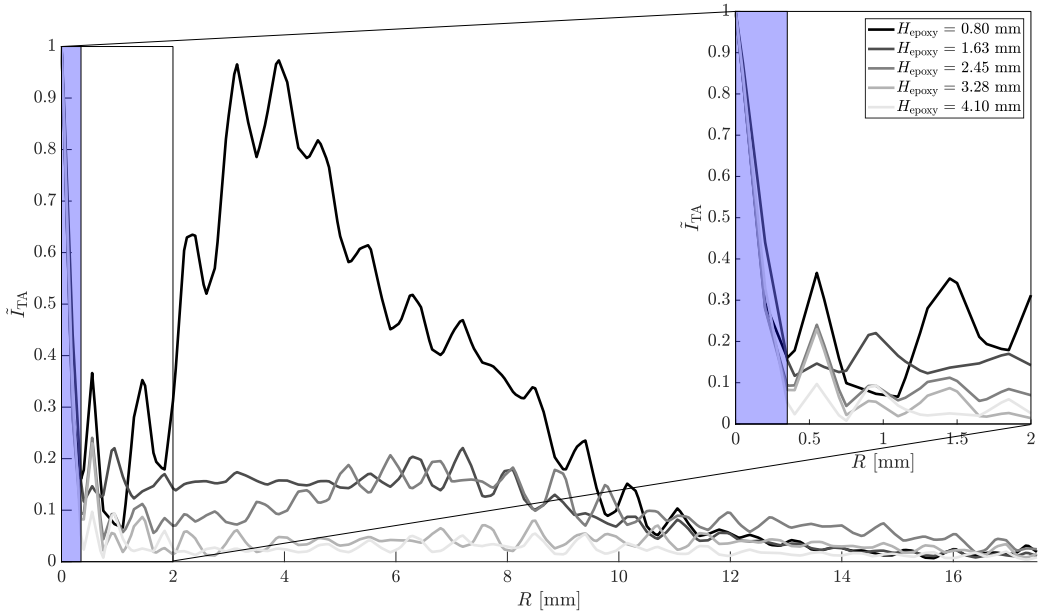

Figure 7: $\tilde{I}_{\mathrm{TA}}$ along the radius for different H_{epoxy}, in the case of the C-lens. The blue area corresponds to the peak area.

3.4. Acoustic intensity distribution inside the Petri dish in the absence of a lens

Figure 8 shows the normalized intensity $\tilde{I}_{\mathrm{TA}}$ inside the Petri dish ($z_{\mathrm{obs}} = 25.81$ mm), which represents the initial configuration without lens (i.e., the experimental set-up developed by Majnooni *et al.* [21]). Here, the *aperture ratio* (defined in Section 2.3.1) is equal to 2.5 %, which means that the beam area represents 2.5

% of the targeted area. The *inhomogeneity* [defined as the mean value and the standard deviation of $|\nabla \tilde{I}_{\mathrm{TA}}|$ (Eq. 10)] is equal to 0.024 ± 0.069 mm^{-1}.

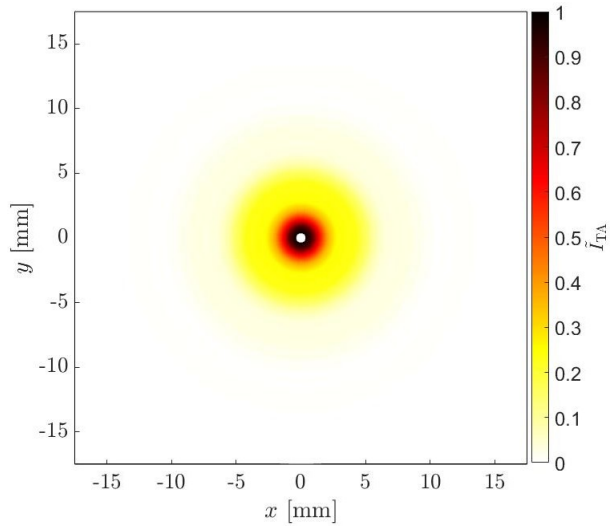

Figure 8: $\tilde{I}_{\mathrm{TA}}$ inside the Petri dish on a plane perpendicular to the z-axis at $z_{\mathrm{obs}} = 25.81$ mm, without lens. The white area in the middle corresponds to the removed peak area (corresponing to the blue area in Fig.7), where the $\tilde{I}_{\mathrm{TA}}$ is set to 0.

3.5. Acoustic intensity distribution inside the Petri dish in the presence of the shaped lens

3.5.1. With the E-lens

Figure 9 shows the distribution of $\tilde{I}_{\mathrm{TA}}$ along the radius of the targeted area ($z_{\mathrm{obs}} = 25.81$ mm, $0 < x < R_{\mathrm{target}} = 17.5$ mm), for the H_{epoxy} values reported in Table 4 for the E-lens.

Figures 12(a) and (d) show the *aperture ratio* values and the *inhomogeneity* for the E-lens, as a function of H_{epoxy} values (Table 4).

For the E-lens, the maximum *aperture ratio* is achieved (43.5 %) for $H_{\mathrm{epoxy}} = 4.25$ mm [Fig.9 and 12(a) and (d)]. The *inhomogeneity* is higher (0.245 ± 0.330 mm^{-1} for $H_{\mathrm{epoxy}} = 4.25$ mm) when the *aperture ratio* is higher (43.5 % for $H_{\mathrm{epoxy}} = 4.25$ mm).

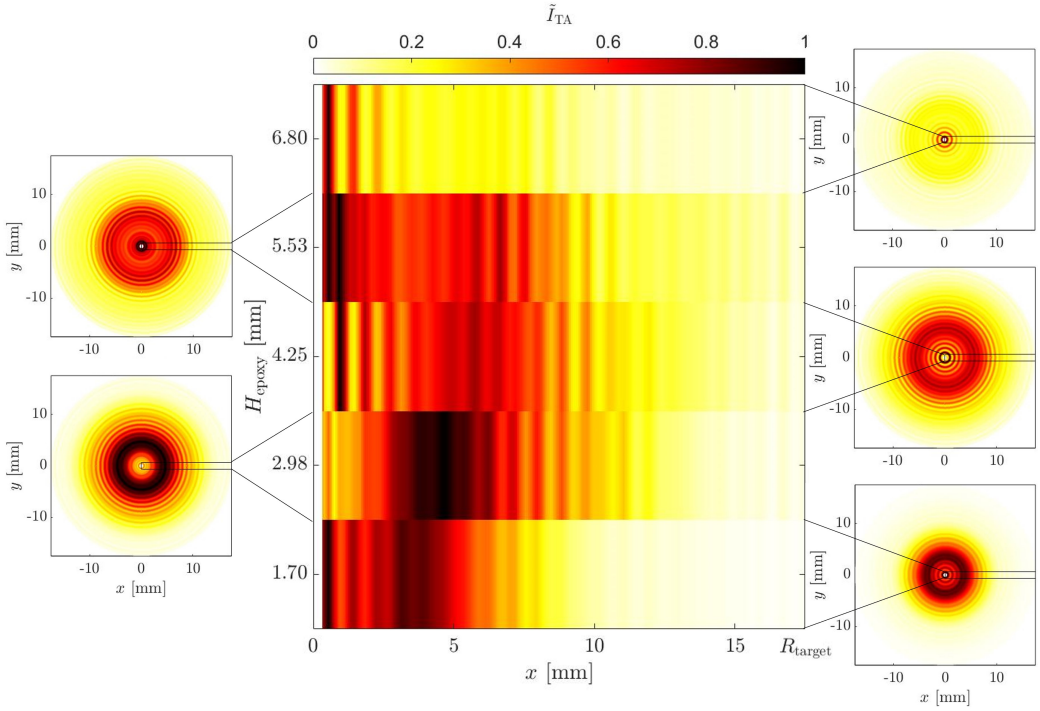

Figure 9: Distribution of the normalized intensity $\tilde{I}_{\mathrm{TA}}$ along the radius of the targeted area ($R_{\mathrm{target}} = 17.5$ mm) for the fixed distance of $z_{\mathrm{obs}} = 25.81$ mm, using the E-lens. In the center (respectively on the left and the right) are shown the half-profile views (respectively the top views of the total areas) for the selected heights H_{epoxy} of the epoxy resin cap (defined in Table 4). The white area (for x between 0 and 0.35 mm) corresponds to the removed peak area (corresponding to the blue area in Fig.7), where the $\tilde{I}_{\mathrm{TA}}$ is set to 0.

3.5.2. With the S-lens

Figure 10 shows the distribution of the normalized intensity $\tilde{I}_{\mathrm{TA}}$ along the radius of the targeted area ($z_{\mathrm{obs}} = 25.81$ mm, $0 < x < R_{\mathrm{target}} = 17.5$ mm), for the H_{epoxy} values reported in Table 4 for the S-lens.

Figures 12(b) and (e) show the *aperture ratio* values and the *inhomogeneity* for the S-lens, as a function of H_{epoxy} values (Table 4).

For the S-lens, the maximum *aperture ratio* is achieved (32.7 %) for $H_{\mathrm{epoxy}} = 3.70$ mm [Fig.10 and 12(b) and (e)]. The corresponding *inhomogeneity* is equal to 0.269 ± 0.337 mm^{-1} . The layer of *PDMS* around the epoxy lens does not improve the *aperture ratio* obtained with the E-lens (-11%) and weakly increases

the *inhomogeneity* of the acoustic intensity distribution (+ 0.012 mm^{-1}).

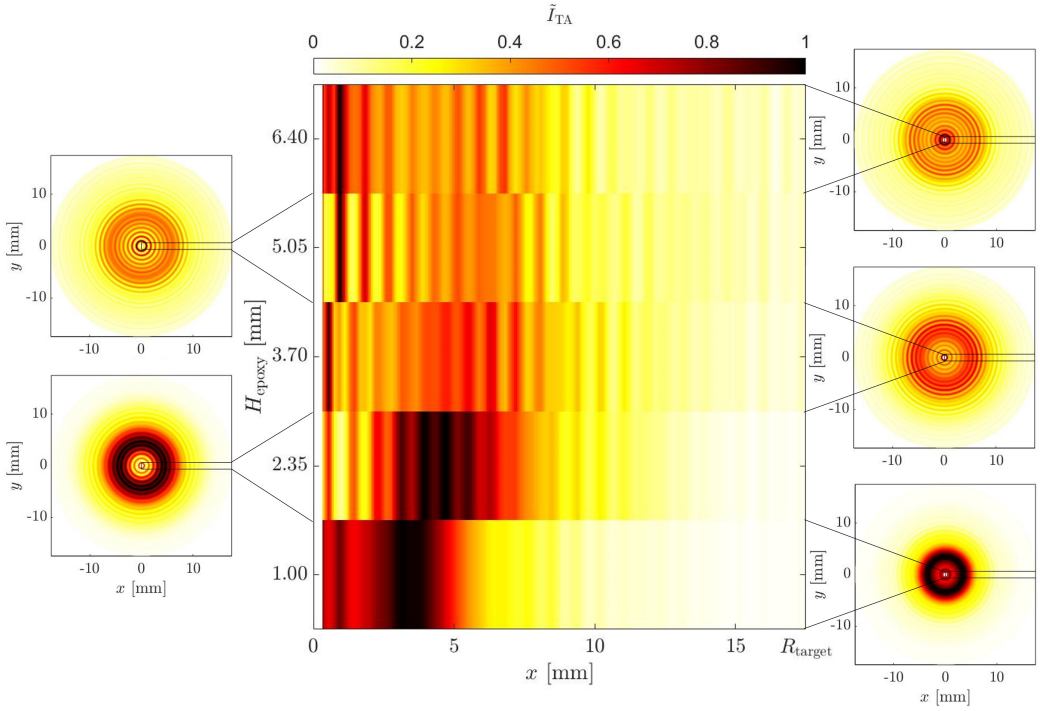

Figure 10: Distribution of the normalized intensity $\tilde{I}_{\mathrm{TA}}$ along the radius of the targeted area ($R_{\mathrm{target}} = 17.5$ mm) for the fixed distance of $z_{\mathrm{obs}} = 25.81$ mm, using the S-lens. In the center (respectively on the left and the right) are shown the half-profile views (respectively the top views of the total areas) for the selected heights H_{epoxy} of the epoxy resin cap. The white area (for x between 0 and 0.35 mm) corresponds to the removed peak area (corresponding to the blue area in Fig.7), where the $\tilde{I}_{\mathrm{TA}}$ is set to 0.

3.5.3. With the C-lens

Figure 11 shows the distribution of the normalized intensity $\tilde{I}_{\mathrm{TA}}$ along the radius of the targeted area ($z_{\mathrm{obs}} = 25.81$ mm, $0 < x < R_{\mathrm{target}} = 17.5$ mm), for the H_{epoxy} values reported in Table 4 for the C-lens.

Figures 12(c) and (f) shows the *aperture ratio* values and the *inhomogeneity* for the C-lens, as a function of H_{epoxy} values (Table 4).

The C-lens achieves coverage of the largest targeted area (67.9%) for $H_{\mathrm{epoxy}} = 2.45$ mm [Fig.11 and 12(c) and 12(f)]. The corresponding *inhomogeneity* is equal to 0.445 ± 0.452 mm^{-1} .

The C-lens can cover most of the targeted area (67.9 %) whereas the E-lens (43.5%) and S-lens (32.7%) cannot even cover half of the targeted area. Nevertheless, the *inhomogeneity* of the acoustic intensity field inside the Petri dish is higher with the C-lens (0.445 ± 0.452 mm^{-1}) than for the E-lens (0.245 ± 0.330 mm^{-1}) and the S-lens (0.269 ± 0.337 mm^{-1}). This non-homogeneity can also be seen more clearly in Fig.11 where, for the highest H_{epoxy} value (4.10 mm), oscillations of $\tilde{I}_{\text{TA}}$ along the radius appear. Those oscillations form rings of different intensities inside the Petri dish.

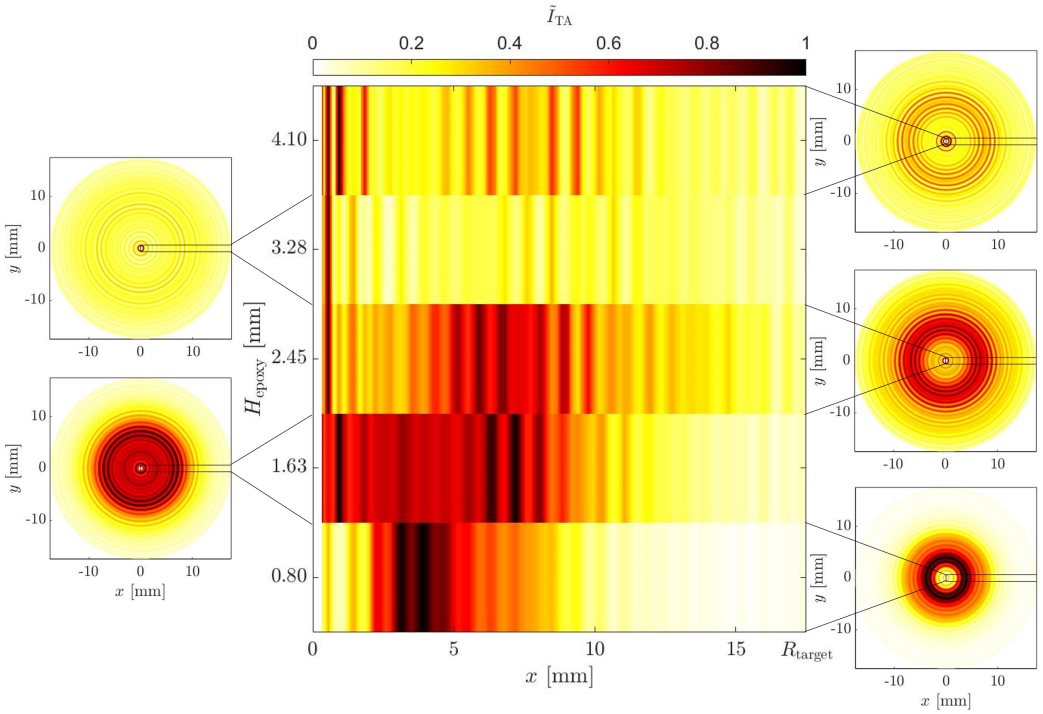

Figure 11: Distribution of the normalized intensity $\tilde{I}_{\text{TA}}$ along the radius of the targeted area ($R_{\text{target}} = 17.5$ mm) for the fixed distance of $z_{\text{obs}} = 25.81$ mm, using the C-lens. In the center (respectively on the left and the right) are show the half-profile views (respectively the top views of the total areas) for the selected heights H_{epoxy} of the epoxy resin cap. The white area (for x between 0 and 0.35 mm) corresponds to the removed peak area (corresponding to the blue area in Fig.7), where the $\tilde{I}_{\text{TA}}$ is set to 0.

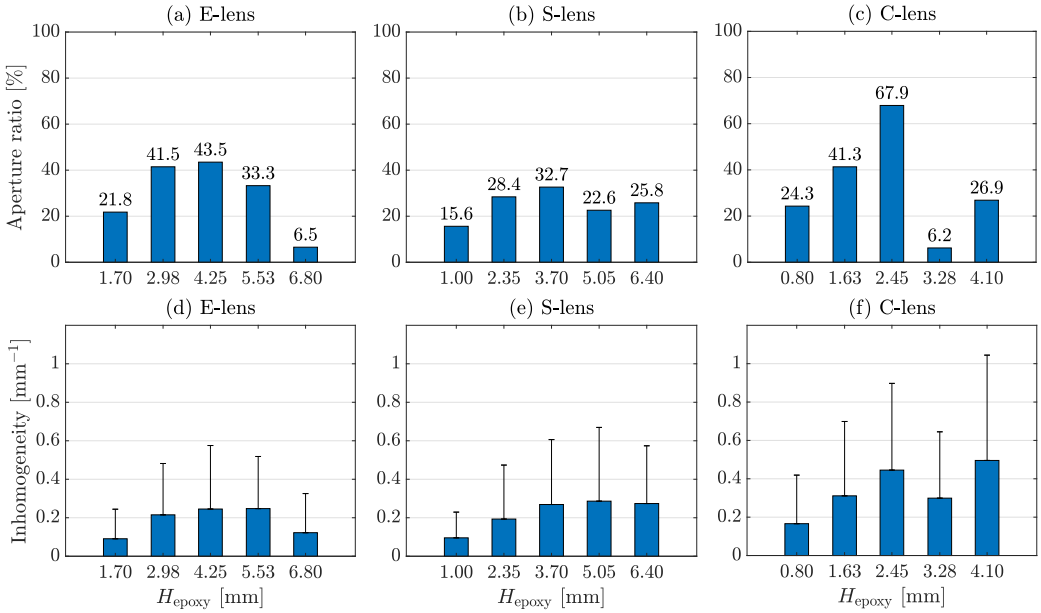

Figure 12: *Aperture ratio* (top diagrams), and *inhomogeneity* (bottom diagrams) for (a) and (d) the E-lens, (b) and (e) the S-lens and (c) and (f) the C-lens, as a function of the values selected for the height H_{epoxy} of the epoxy resin cap (Table 4).

3.6. Acoustic pressure loss

Figure 13 shows the *acoustic pressure loss* for each shape of lens, along a path followed by a ray starting at the edge of the transducer $x = D_{\text{td}}/2 = 6.5$ mm. This ray passes through the two components of the S-lens and C-lens, which allows us to investigate the attenuation effect of the material each component is made of (epoxy and *PDMS*).

Inside the E-lens, multiple wave reflections, due to the high impedance contrast between epoxy resin and water, occur at the boundaries. Moreover, the attenuation of the compression waves is high in the epoxy resin. The combination of these two phenomena results in an *acoustic pressure loss* that increases as a function of H_{epoxy}, from 0.3 dB for a height of 1.70 mm to 1.7 dB for a height of 6.80 mm. To counteract these effects, the epoxy resin cap was surrounded by a *PDMS* layer, allowing the acoustic impedance between the epoxy resin cap and the water to be better matched.

For the S-lens, Figure 13(b) shows that the *acoustic pressure loss* is the same as for the E-lens, for a slightly lower H_{epoxy} height. In addition, most of the

acoustic pressure loss is due to the epoxy resin cap (88%), and not to the *PDMS* layer which attenuates the waves less (11%).

For the C-lens, the *PDMS* layer is thicker at the extremities of the lens. This cylindrical shape allows the increase of the *aperture ratio*, but the most diffracted ultrasonic waves on the edges of the epoxy resin cap are propagated through a greater thickness of *PDMS*, and are thus more attenuated [Figure 13(c)]. Indeed, the loss due to the *PDMS* layer of the lens is close to the one due to the epoxy resin cap of the lens ($\approx 50\%$).

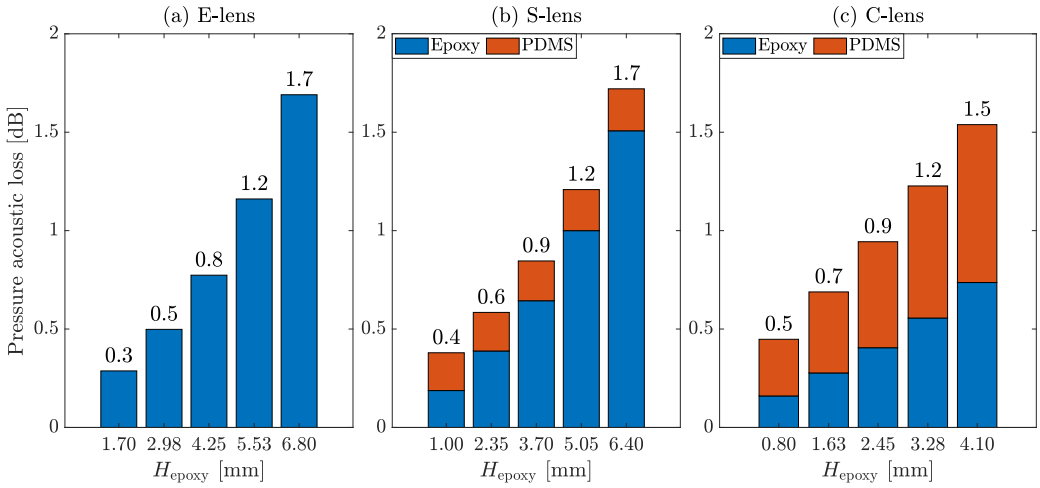

Figure 13: *Acoustic pressure loss* at the distance $x = D_{\text{td}}/2 = 6.5$ mm from the center of the transducer, along the transducer radius, in (a) an E-lens, (b) a S-lens and (c) a C-lens, as a function of the values selected for the height H_{epoxy} of the epoxy resin cap (Table 4). The blue bars represent the *acoustic pressure loss* due to the epoxy resin cap and the red bars the one due to the *PDMS* layer.

The energy transmitted through the lens depends also of the reflection and transmission coefficients (given in Appendix B under normal incident conditions) at each material interface. For the E-lens, the only interface is between epoxy and water, which gives a transmission coefficient of $T_{\text{epoxy, water}} = 0.93$ and a reflection coefficient of $R_{\text{epoxy, water}} = 0.07$ (using the material properties given in Table 2). For the S-lens and the C-lens, there are two interfaces: the first one between epoxy and *PDMS* gives a transmission coefficient of $T_{\text{epoxy, }PDMS} = 0.84$ and a reflection coefficient of $R_{\text{epoxy, }PDMS} = 0.16$, and the second one between *PDMS* and water gives transmission coefficient of $T_{PDMS, \text{ water}} = 0.97$ and a reflection

coefficient of $R_{PDMS,\,\text{water}} = 0.03$, which leads to a total transmission coefficient of $T_{\text{epoxy},\,PDMS} \times T_{PDMS,\,\text{water}} = 0.81$. As the transmission coefficient of the E-lens is higher than the one of the S-lens and C-lens, it means that more energy is transmitted through the E-lens. However, those coefficients are calculated under normal incident conditions, which is the case only at the center of each lens. Anywhere else along the radius of the lens, the incident angle varies, which varies the reflection and transmission coefficients at each interface [33].

3.7. Summary

In order to summarize all those results, let us compare the results obtained for different lenses that give the same *aperture ratios*.

3.7.1. The E-lens and the C-lens

Table 5 summarizes the different results obtained for an E-lens and a C-lens that give an *aperture ratio* of 41%. In this case, the best choice would be the E-lens because it reduces the *inhomogeneity* (-30%) ant it leads to a smaller *acoustic pressure loss* than the C-lens. It is also a lens easier to make because it is made of epoxy only.

Shape of lens	E-lens	C-lens
H_{epoxy} [mm]	2.98	1.63
Aperture ratio [%]	41.5	41.3
Inhomogeneity [mm^{-1}]	0.215 ± 0.267	0.311 ± 0.388
Acoustic pressure loss [dB]	0.5	0.7

Table 5: H_{epoxy}, *inhomogeneity* and *acoustic pressure loss* for an E-lens and a C-lens that achieve an *aperture ratio* of 41%

3.7.2. The E-lens and the S-lens

Table 6 summarizes the different results obtained for an E-lens and a S-lens that give an *aperture ratio* of 33%. In this case, the E-lens would still be a better choice because it reduces the *inhomogeneity* a little more than the S-lens (-8%). The drawback is that the *acoustic pressure loss* is a little higher (+0.3 dB).

Shape of lens	E-lens	S-lens
H_{epoxy} [mm]	5.53	3.70
Aperture ratio [%]	33.3	32.7
Inhomogeneity [mm^{-1}]	0.248 ± 0.271	0.269 ± 0.337
Acoustic pressure loss [dB]	1.2	0.9

Table 6: H_{epoxy}, *inhomogeneity* and *acoustic pressure loss* for an E-lens and a S-lens that achieve an *aperture ratio* of 33%

3.7.3. The S-lens and the C-lens

Table 7 summarizes the different results obtained for a S-lens and a C-lens that give an *aperture ratio* around 25%. For this particular *aperture ratio*, both the smallest ($H_{\text{Epoxy}} = 0.80$ mm) and the highest ($H_{\text{Epoxy}} = 4.10$ mm) C-lenses work, but they give different results. The smallest C-lens gives the smallest *inhomogeneity* (-66%) and the smallest *acoustic pressure loss* (-1 dB) in comparison with the highest C-lens. The *inhomogeneity* is also reduced in comparison with the S-lens (-40%).

Shape of lens	S-lens	C-lens	
H_{epoxy} [mm]	6.40	4.10	0.80
Aperture ratio [%]	25.8	26.9	24.3
Inhomogeneity [mm^{-1}]	0.274 ± 0.300	0.496 ± 0.549	0.166 ± 0.253
Acoustic pressure loss [dB]	1.7	1.5	0.5

Table 7: H_{epoxy}, *inhomogeneity* and *acoustic pressure loss* for an E-lens and a S-lens that achieve an *aperture ratio* around 25%

If the purpose of using the lens is only to increase the *aperture ratio* as much as possible, the best choice would be the C-lens. However it also increases the *inhomogeneity*. By contrast, if an *aperture ratio* of 40% is enough, the E-lens would provide a better homogeneity of the acoustic intensity distribution inside the Petri dish. Finally, the use of a S-lens does not improve anything: the *aperture ratio* is smaller than with an E-lens and the *inhomogeneity* is higher.

4. Conclusion

This work proposes a computational *FEM*-model to guide the design of acoustic lenses in terms of size and shape, with the objective of ensuring a homogeneous ultrasound stimulation on the whole cell culture area inside a Petri dish, within the framework of *LIPUS* stimulation of bone cells. Three different lens shapes based on an epoxy resin part with various heights covered with a *PDMS* layer were studied. Lens efficiency was quantified in terms of field aperture, homogeneity of the acoustic intensity distribution inside the Petri dish and attenuation due to the lens.

There is no ideal lens configuration that homogenizes the field and distributes the acoustic intensity to the whole targeted area. The design of the lens should be a compromise which depends on the priority given to the 2 criteria related to the biological effects induced. For example, if it is only used to enlarge the acoustic field, the C-lens is the best choice, but it will lead to a less homogeneous acoustic intensity distribution and to more attenuation. Then, more attenuation means increased voltage input, which may damage the transducer.

The computational model we developed allowed us to access parameters the experimental measurements of which are complicated, such as the acoustic intensity at the cells level. It also allowed us to test different configurations, such as the geometry of the lens, its composition, the excitation frequency, etc..., in order to eliminate the irrelevant configurations that will not be experimentally tested. The next step will be to make the lens and to measure its effect on the acoustic field, in order to compare it with the corresponding simulated one to validate the computational model.

Acknowledgments

The project leading to this publication has received funding from the CNRS project AAP2017-OSEZ-BARON, and the Excellence Initiative of Aix-Marseille University - A*Midex, a French “Investissements d’Avenir programme” - Institut Mécanique et Ingénierie (IMI, AMX-19-IET-010). The authors would like to thank Julien Deschamps and Eric Bertrand of the Institute for Research on Non-Equilibrium Phenomena (IRPHE) for their help with *PDMS*, and Marie-Hélène Mignard for English language revision.

Appendix A. Acoustic intensities and gradient

In the design and development of *US* medical applications, the acoustic intensity, which is defined as the rate of energy transfer per unit time per unit area

[W/m^2], is a key parameter [34]. In a fluid, it is given by the time average of the product between the acoustic pressure $p(t)$ and the particle velocity $u(t)$ over the period of oscillations T [35]:

$$I = \lim_{T\to\infty} \frac{1}{T} \int_0^T p(t)u(t)\mathrm{d}t \ . \tag{A.1}$$

For a harmonic wave, the acoustic intensity can be written as follows:

$$I = \frac{1}{2}\Re[p(t)u(t)^*], \text{ with } \begin{cases} p(t) = P_0 \mathrm{e}^{-\mathrm{i}(\omega t - \phi)} \\ u(t) = U_0 \mathrm{e}^{-\mathrm{i}(\omega t - \phi)} \end{cases} \tag{A.2}$$

where * denotes the complex conjugate and $\Re$, the real part.

Different parameters can be calculated, in order to characterize the acoustic field, such as:

- the *Temporal Average Intensity* (I_{TA});
- the *Spatial Peak Temporal Average Intensity* (I_{SPTA}) corresponding to the maximum value of I_{TA} over the beam cross-sectional area S;
- the *Spatial Average Time Average Intensity* (I_{SATA}), which corresponds to the I_{TA} averaged over the surface S;
- the ratio of surface covered by at least 25% I_{SPTA} over the surface S [22]. It corresponds to a level of attenuation of -6dB, which is the threshold defining the active area of a plane transducer;
- the mean value and standard deviation of the absolute value of the gradient of the normalized I_{TA} ($\tilde{I}_{\mathrm{TA}}$) [15]. They represent the variation of the intensity field (the *inhomogeneity* of the field): the smaller the mean gradient, the flatter the intensity field.

In the case of a pulsed signal, the *Pulse-Intensity Integral* I_{PI} is written as follows ([22], p.96):

$$I_{\mathrm{PI}} = P_{\mathrm{I}}/Z \ , \tag{A.3}$$

with P_{I}, the *Pulse-Pressure-Squared Integral*, defined as follows ([22], p.93):

$$P_{\mathrm{I}} = \int_0^{T_{\mathrm{PRP}}} p(t)^2 \mathrm{d}t \ , \tag{A.4}$$

where T_{PRP} is the *Pulse Repetition Period*, which corresponds to the total duration of the signal, including the pulse duration.

Then, the *Temporal-Average Intensity* I_{TA} is written as follows ([22], p.97):

$$I_{\mathrm{TA}} = F_{\mathrm{PRF}} I_{\mathrm{PI}} \ , \tag{A.5}$$

where $F_{\mathrm{PRF}} = 1/T_{\mathrm{PRP}}$ is the *Pulse Repetition Frequency*.

Finally, when reporting Eq. (A.4) into Eq. (A.5), we obtain:

$$I_{\mathrm{TA}} = 1/(ZT_{\mathrm{PRP}}) \int_0^{T_{\mathrm{PRP}}} p(t)^2 \mathrm{d}t \ . \tag{A.6}$$

From the I_{TA}, the *Spatial Peak Temporal Average Intensity* I_{SPTA} is given by ([22], p.98):

$$I_{\mathrm{SPTA}} = \max_S (I_{\mathrm{TA}}) \ , \tag{A.7}$$

where S corresponds to the beam cross-sectional area.

The *Spatial Average Time Average Intensity* I_{SATA} can then be defined as [36]:

$$I_{\mathrm{SATA}} = 1/A_6 \iint_{S_6} I_{\mathrm{TA}}(r) \mathrm{d}S \ , \tag{A.8}$$

where $I_{\mathrm{TA}}(r)$ is the I_{TA} at the point defined by the coordinate vector r on the surface S. The integral limit S_6 represents the integration over the surface where the I_{TA} is greater than 25% I_{SPTA} (-6 dB), and A_6 is the -6 dB beam cross-sectional area (which corresponds to the active beam diameter).

The normalized I_{TA} is written as follows:

$$\tilde{I}_{\mathrm{TA}} = I_{\mathrm{TA}} / I_{\mathrm{SPTA}} \ , \tag{A.9}$$

and its gradient is given by:

$$\nabla \tilde{I}_{\mathrm{TA}} = \frac{\partial \tilde{I}_{\mathrm{TA}}}{\partial x} \vec{x} + \frac{\partial \tilde{I}_{\mathrm{TA}}}{\partial y} \vec{y} \ . \tag{A.10}$$

The absolute value of the gradient of the $\tilde{I_{\mathrm{TA}}}$ is:

$$\left| \nabla \tilde{I}_{\mathrm{TA}} \right| = \left| \frac{\partial \tilde{I}_{\mathrm{TA}}}{\partial x} \right| + \left| \frac{\partial \tilde{I}_{\mathrm{TA}}}{\partial y} \right| \ . \tag{A.11}$$

Finally, the *inhomogeneity* is characterized by the mean value and the standard deviation of $\left| \nabla \tilde{I}_{\mathrm{TA}} \right|$.

Appendix B. Reflection and transmission coefficients

The reflection coefficient of a wave on a medium 1/medium 2 interface is defined under normal incident conditions as:

$$R_{1,2} = \frac{(Z_2 - Z_1)^2}{(Z_2 + Z_1)^2} \,, \tag{B.1}$$

and the transmission coefficient is defined as:

$$T_{1,2} = \frac{4Z_1 Z_2}{(Z_2 + Z_1)^2} \,, \tag{B.2}$$

where $Z_1 = \rho_1 c_1$ and $Z_2 = \rho_2 c_2$ are the acoustic impedance (expressed in MRayls) of medium 1 and of medium 2 respectively. ρ is the mass density of the medium and c is the compression wave velocity of the medium.

References

[1] P. Laugier, Q. Grimal (Eds.), Bone Quantitative Ultrasound: New Horizons, Vol. 1364 of Advances in Experimental Medicine and Biology, Springer International Publishing, Cham, 2022. doi:10.1007/978-3-030-91979-5.

[2] C. L. Romano, D. Romano, N. Logoluso, Low-Intensity Pulsed Ultrasound for the Treatment of Bone Delayed Union or Nonunion: A Review, Ultrasound in Medicine & Biology 35 (4) (2009) 529–536. doi:10.1016/j.ultrasmedbio.2008.09.029.

[3] V. Buchtala, The present state of ultrasonic therapy, Br. J. Phys. Med. 15 (1) (1952) 3–6.

[4] R. Zura, G. J. Della Rocca, S. Mehta, A. Harrison, C. Brodie, J. Jones, R. G. Steen, Treatment of chronic (>1 year) fracture nonunion: Heal rate in a cohort of 767 patients treated with low-intensity pulsed ultrasound (LIPUS), Injury 46 (10) (2015) 2036–2041. doi:10.1016/j.injury.2015.05.042.

[5] R. Leighton, J. T. Watson, P. Giannoudis, C. Papakostidis, A. Harrison, R. G. Steen, Healing of fracture nonunions treated with low-intensity pulsed ultrasound (LIPUS): A systematic review and meta-analysis, Injury 48 (7) (2017) 1339–1347. doi:10.1016/j.injury.2017.05.016.

[6] C. L. Romanò, A. Kirienko, C. Sandrone, G. Toro, A. Toro, E. P. Valente, M. Caporale, M. Imbimbo, G. Falzarano, S. Setti, E. Meani, Low-Intensity Pulsed Ultrasound in the Treatment of Nonunions and Fresh Fractures: A Case Series, Trauma Care 2 (2) (2022) 174–184. doi:10.3390/traumacare2020014.

[7] P. Nolte, R. Anderson, E. Strauss, Z. Wang, L. Hu, Z. Xu, R. G. Steen, Heal rate of metatarsal fractures: A propensity-matching study of patients treated with low-intensity pulsed ultrasound (LIPUS) vs. surgical and other treatments, Injury 47 (11) (2016) 2584–2590. doi:10.1016/j.injury.2016.09.023.

[8] K. H. Teoh, R. Whitham, J. F. Wong, K. Hariharan, The use of low-intensity pulsed ultrasound in treating delayed union of fifth metatarsal fractures, The Foot 35 (2018) 52–55. doi:10.1016/j.foot.2018.01.004.

[9] R. Anderson, S. Parekh, M. J. Braid-Forbes, R. G. Steen, Delayed Healing in Metatarsal Fractures: Role of Low-Intensity Pulsed Ultrasound Treatment, The Journal of Foot and Ankle Surgery 58 (2019) 1145–1151. doi:10.1053/j.jfas.2019.03.010.

[10] J. W. Busse, J. Kaur, B. Mollon, M. Bhandari, P. Tornetta, H. J. Schunemann, G. H. Guyatt, Low intensity pulsed ultrasonography for fractures: systematic review of randomised controlled trials, BMJ 338 (feb27 1) (2009) b351–b351. doi:10.1136/bmj.b351.

[11] S. Schandelmaier, A. Kaushal, L. Lytvyn, D. Heels-Ansdell, R. A. C. Siemieniuk, T. Agoritsas, G. H. Guyatt, P. O. Vandvik, R. Couban, B. Mollon, J. W. Busse, Low intensity pulsed ultrasound for bone healing: systematic review of randomized controlled trials, BMJ 356 (2017). doi:10.1136/bmj.j656.

[12] P. Martinez de Albornoz, A. Khanna, U. G. Longo, F. Forriol, N. Maffulli, The evidence of low-intensity pulsed ultrasound for in vitro, animal and human fracture healing, British Medical Bulletin 100 (1) (2011) 39–57. doi:10.1093/bmb/ldr006.

[13] F. Fontana, F. Iberite, A. Cafarelli, A. Aliperta, G. Baldi, E. Gabusi, P. Dolzani, S. Cristino, G. Lisignoli, T. Pratellesi, E. Dumont, L. Ricotti, Development and validation of low-intensity pulsed ultrasound systems for

highly controlled in vitro cell stimulation, Ultrasonics 116 (2021) 106495. doi:10.1016/j.ultras.2021.106495.

[14] J.-S. Sun, R.-C. Hong, W. H.-S. Chang, L.-T. Chen, F.-H. Lin, H.-C. Liu, In vitro effects of low-intensity ultrasound stimulation on the bone cells, J. Biomed. Mater. Res. 57 (3) (2001) 449–456. doi:10.1002/1097-4636(20011205)57:3<449::AID-JBM1188>3.0.CO;2-0.

[15] D. A. Horne, P. D. Jones, M. S. Adams, J. C. Lotz, C. J. Diederich, LIPUS far-field exposimetry system for uniform stimulation of tissues *in-vitro* : development and validation with bovine intervertebral disc cells, Biomed. Phys. Eng. Express 6 (3) (2020) 035033. doi:10.1088/2057-1976/ab8b26.

[16] Y.-C. Tien, S.-D. Lin, C.-H. Chen, C.-C. Lu, S.-J. Su, T.-T. Chih, Effects of Pulsed Low-Intensity Ultrasound on Human Child Chondrocytes, Ultrasound in Medicine & Biology 34 (7) (2008) 1174–1181. doi:10.1016/j.ultrasmedbio.2007.12.019.

[17] F. Padilla, R. Puts, L. Vico, K. Raum, Stimulation of bone repair with ultrasound: A review of the possible mechanic effects, Ultrasonics 54 (5) (2014) 1125–1145. doi:10.1016/j.ultras.2014.01.004.

[18] W. Secomski, K. Bilmin, T. Kujawska, A. Nowicki, P. Grieb, P. A. Lewin, In vitro ultrasound experiments: Standing wave and multiple reflections influence on the outcome, Ultrasonics 77 (2017) 203–213. doi:10.1016/j.ultras.2017.02.008.

[19] M. Snehota, J. Vachutka, G. ter Haar, L. Dolezal, H. Kolarova, Therapeutic ultrasound experiments in vitro: Review of factors influencing outcomes and reproducibility, Ultrasonics 107 (2020) 106167. doi:10.1016/j.ultras.2020.106167.

[20] M. Majnooni, E. Doveri, J. Baldisser, V. Long, J. Houles, J.-C. Scimeca, D. Momier, C. Guivier-Curien, P. Lasaygues, C. Baron, Anti-reflection cover to control acoustic intensity in *in vitro* low-intensity ultrasound stimulation of cells, Acta Acust. 6 (2022) 11. doi:10.1051/aacus/2022007.

[21] M. Majnooni, P. Lasaygues, V. Long, J.-C. Scimeca, D. Momier, F. Rico, N. Buzhinsky, C. Guivier-Curien, C. Baron, Monitoring of in-vitro ultrasonic

stimulation of cells by numerical modeling, Ultrasonics 124 (2022) 106714. doi:10.1016/j.ultras.2022.106714.

[22] R. C. Preston (Ed.), Output Measurements for Medical Ultrasound, Springer London, London, 1991. doi:10.1007/978-1-4471-1883-1.

[23] K. Waters, M. Hughes, J. Mobley, J. Miller, Differential forms of the Kramers-Kronig dispersion relations, IEEE Trans. Ultrason., Ferroelect., Freq. Contr. 50 (1) (2003) 68–76. doi:10.1109/TUFFC.2003.1176526.

[24] S. Yang, W. Qin, H. Guo, T. Jin, N. Huang, M. He, L. Xi, Design and evaluation of a compound acoustic lens for photoacoustic computed tomography, Biomed. Opt. Express 8 (5) (2017) 2756. doi:10.1364/BOE.8.002756.

[25] G. Xu, Z. Ni, X. Chen, J. Tu, X. Guo, H. Bruus, D. Zhang, Acoustic Characterization of Polydimethylsiloxane for Microscale Acoustofluidics, Phys. Rev. Applied 13 (5) (2020) 054069. doi:10.1103/PhysRevApplied.13.054069.

[26] Y. Wang, R. Challis, A.-Y. Phang, M. Unwin, Bulk shear wave propagation in an epoxy: attenuation and phase velocity over five decades of frequency, IEEE Trans. Ultrason., Ferroelect., Freq. Contr. 56 (11) (2009) 2504–2513. doi:10.1109/TUFFC.2009.1337.

[27] Nonlinear Acoustics - Modeling of the 1D Westervelt Equation, COMSOL Multiphysics v.5.5, Stockholm, Sweden (2021).
URL https://www.comsol.com/model/nonlinear-acoustics-8212-modeling-of-the-1d-westervelt-equation-12783

[28] P. Jordan, R. Keiffer, Comments on: "On the sound attenuation in fluid due to the thermal diffusion and viscous dissipation" [Phys. Lett. A 379 (2015) 1799–1801], Physics Letters A 380 (14-15) (2016) 1392–1393. doi:10.1016/j.physleta.2016.01.050.

[29] L. D. Landau, E. M. Lifshitz, Fluid Mechanics: Volume 6., Elsevier Science, 1987.

[30] M. Engholm, C. Beers, H. Bouzari, J. A. Jensen, E. V. Thomsen, Increasing the field-of-view of row–column-addressed ultrasound transducers: implementation of a diverging compound lens, Ultrasonics 88 (2018) 97–105. doi:10.1016/j.ultras.2018.02.001.

[31] K. Hensel, M. P. Mienkina, G. Schmitz, Analysis of Ultrasound Fields in Cell Culture Wells for In Vitro Ultrasound Therapy Experiments, Ultrasound in Medicine & Biology 37 (12) (2011) 2105–2115. doi:10.1016/j.ultrasmedbio.2011.09.007.

[32] G. Tamboia, M. Campanini, V. Vighetto, L. Racca, L. Spigarelli, G. Canavese, V. Cauda, A comparative analysis of low intensity ultrasound effects on living cells: from simulation to experiments, Biomed Microdevices 24 (4) (2022) 35. doi:10.1007/s10544-022-00635-x.

[33] M. A. Ainslie, Plane-wave reflection and transmission coefficients for a three-layered elastic medium, The Journal of the Acoustical Society of America 97 (2) (1995) 954–961. doi:10.1121/1.412074.

[34] FDA, 501(k) Guide for Measuring and Reporting Acoustic Output of Diagnostic Ultrasound Medical Devices, US Department of Health and Human Services, FDA Rockville, MD (1985).

[35] D. Royer, E. Dieulesaint, Elastic waves in solids I: Free and Guided Propagation, Advanced texts in physics, Springer, Berlin ; New York, 1999.

[36] P. Acevedo, D. Das-Gupta, The measurement of the spatial average temporal average intensity Isata and ultrasonic power W in composite ultrasonic transducers for medical application, Ultrasonics 40 (1-8) (2002) 819–821. doi:10.1016/S0041-624X(02)00218-4.